Chapter 7

Corrosion Behavior

In this chapter, the corrosion behavior of squeeze-cast Mg-5.0Al-2.0Ca-0.3Mn (wt.%) (AXM520) alloy and nanocomposites are investigated by hydrogen evolution, and potentiodynamic polarization methods in an aqueous NaCl solution. The corrosion products and corroded surfaces are analyzed with the help of X-ray Diffraction (XRD), Scanning Electron Microscopy (SEM), and X-ray photoelectron spectroscopy (XPS). The corrosion behavior of the alloy and NCs is correlated with their initial as-cast microstructures. A summary of the corrosion work is presented at the end of this chapter.

7.1 Hydrogen evolution and immersion tests

Mg undergoes corrosion by reacting with water and emit H_2 gas as per the below equation [124]:

$$Mg + 2H_2O \rightarrow Mg(OH)_2 + H_2 \uparrow \qquad \text{Equation 7.1}$$

The results of hydrogen evolution tests for AXM520 alloy and NCs following 60 h of immersion in NaCl are plotted in Figure 7.1(a). The H_2 evolution for the alloy and NCs accelerated with the passing immersion time. The H_2 evolution of the individual NC remains lower than the alloy. Figure 7.1(b) presents the corrosion rates assessed from the immersion tests. The NCs exhibit a lower rate of corrosion than that of AXM520 alloy for the entire duration. Thus, the incorporation of SiC_{np} caused a reduced corrosion rate of NCs. Further, the corrosion rate gradually diminished with the rise in SiC_{np} concentration in the alloy. The lowest corrosion rate was exhibited by NC3.0SiC. The corrosion rates (mm/yr) of the AXM520 and NC3.0SiC obtained from the current study are compared with the values previously reported for the various Mg-Al-based alloys and their composites in Table 7.1. The newly developed NCs in the current study displayed significantly greater resistance during corrosion relative to the published values. The corrosion rates of the AXM520 and NCs calculated from the weight loss measurements are shown in Figure 7.1(c and d). The results of immersion tests reconfirm the trend observed in the corrosion rates observed in the hydrogen evolution tests for the alloy and NCs. The NCs exhibited lower rates of corrosion than the AXM520 alloy for the entire duration. In addition, the corrosion rate gradually diminished with the increase in SiC_{np} concentration in the alloy.

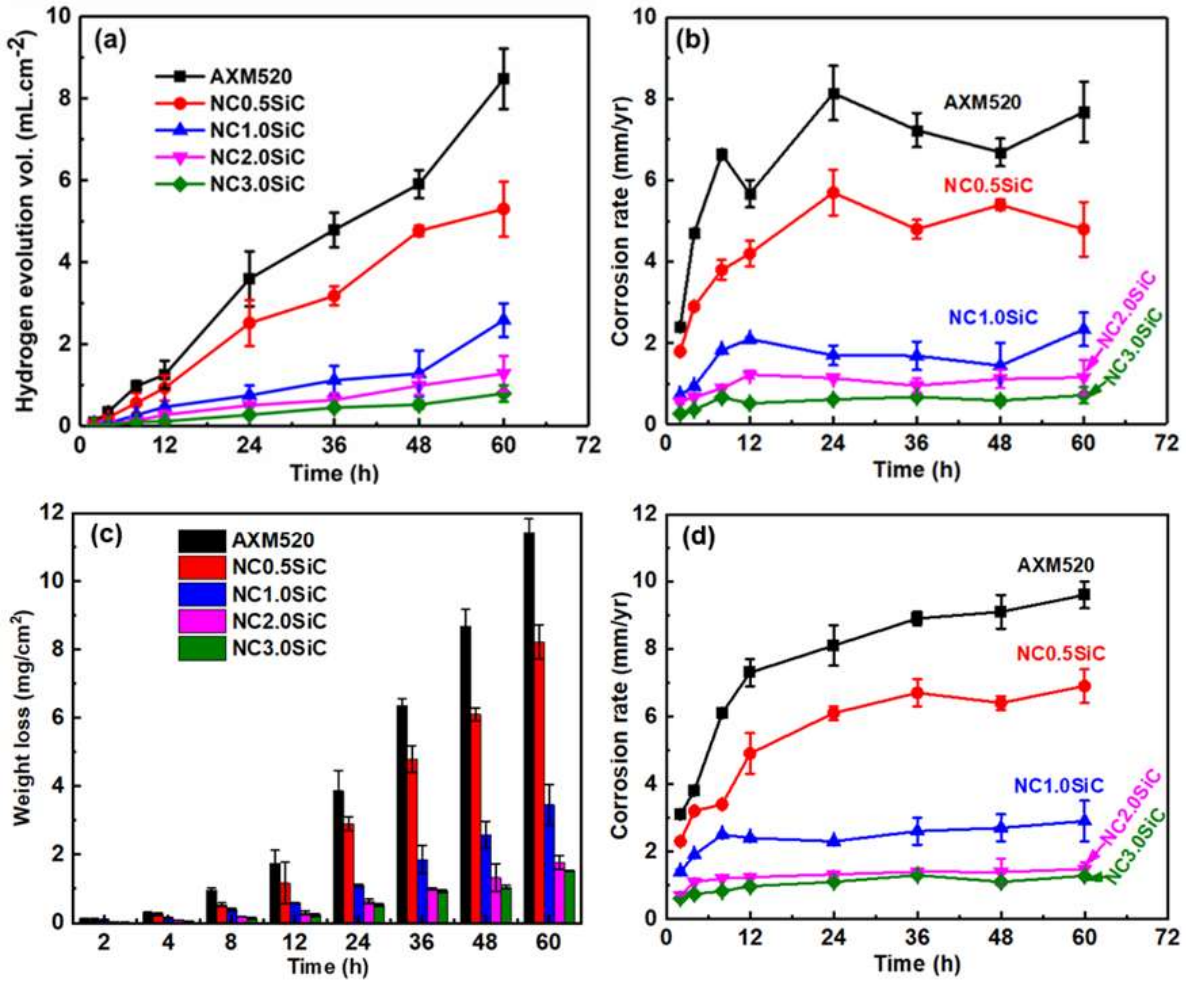

Figure 7.1 (a) Hydrogen evolution as a function of time, (b) corrosion rate calculated from 'a' for AXM520 and NCs, (c) weight loss of the alloy and NCs as a function of time, and (d) corrosion rates calculated from 'c'.

Table 7.1 A comparison of corrosion rates evaluated from H_2 evaluation tests in the present study with that obtained on various Mg-Al-based alloys and their composites.

Materials	Fabrication Process	Corrosion medium	Immersion time (h)	Corrosion rate (mm/yr)	Ref.
AZXY9120+ 2.0 wt. SiC_{np}	Squeeze casting	0.1 (M) NaCl Soln.	10	102.00±1.30	[44]
AZXB9120	Squeeze casting	0.1 (M) NaCl Soln.	12	69.20±2.40	[125]
AZ91+2.0 (wt.%) GNP	Squeeze casting + 20 s ultrasonic shot peening	0.1 (M) NaCl Soln.	12	20.00±1.70	[126]
Mg-1.0Al-0.3Ca	Extruded and heat treated at T6 200 ºC for 4 h	0.6 (M) NaCl Soln.	48	4.36±0.77	[127]
AXM520	Squeeze casting	0.6 (M) NaCl Soln.	60	7.08±0.85	This work
AXM520+3.0 (wt.%) SiC_{np}	Squeeze casting	0.6 (M) NaCl Soln.	60	0.63±0.13	This work

7.2 Open circuit potential (OCP)

The results from the OCP tests of the AXM520 and fabricated NCs are plotted in Figure 7.2. Following an initial small variation, the OCP of all the materials achieved a steady state, and it was attributed to a stable corrosion layer formation on the surfaces of the alloy and NCs [44]. The OCP values shifted more to the positive voltage (E_{OCP}) as the wt.% of nanoparticles gradually raised in the AXM520 alloy. The average OCP values for all the tested materials assessed from the curves in Figure 7.2 are summarized in Table 7.2. The AXM520 alloy exhibited the lowest E_{OCP} (i.e., -1559.7 ± 4.8 mV) among the materials employed. The OCP values of all the NCs were higher in contrast to the alloy, and the values gradually became bigger with the increased wt.% of the SiC_{np} content in NCs. Among the NCs, the lowest E_{OCP} (i.e., -1538.2 ± 5.3 mV) and highest (i.e., -1453.1 ± 5.3 mV) values were exhibited by NC0.5SiC and NC3.0SiC, respectively. The E_{OCP} values for the NC1.0SiC and NC2.0SiC were

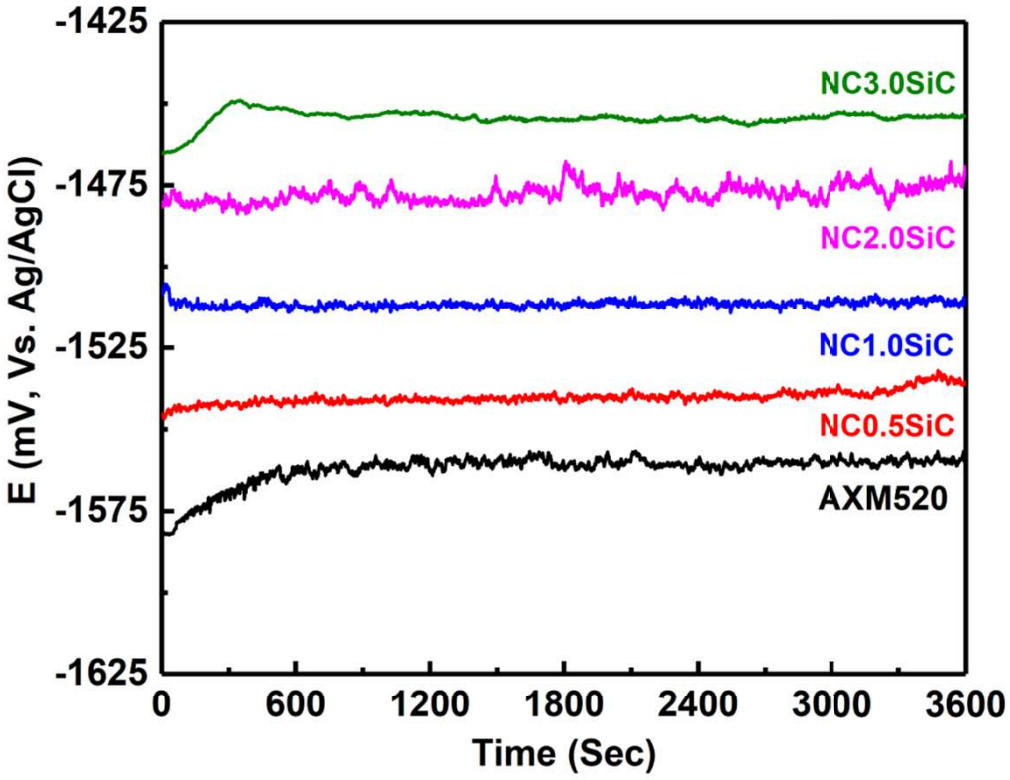

Figure 7.2 Variation of OCP recorded as a function of time for all the materials tested.

-1511.5 ± 2.7 and -1474.3 ± 6.7 mV, respectively. Thus, the NC3.0SiC was the noblest among the NCs, and it exhibited a 6.8% improvement in E_{OCP} value compared to the AXM520 alloy.

7.3 EIS studies

Figure 7.3(a) exhibits the Nyquist plots for as-cast AXM520 and NCs. The loop radius of the curve obtained from the AXM520 alloy was the smallest, and it was bigger for all the NCs, indicating the corrosion resistance was the lowest for the alloy. The loop radius increased with the increase in SiC_{np} in the NCs, which suggests that the corrosion resistance of NCs enhanced as wt.% of SiC_{np} is increased in them. Among the NCs, the loop radius was the highest for NC3.0SiC and lowest for NC0.5SiC. The presence of an inductive loop at the low-frequency domain signifies the adsorption and decomposition of ions due to the reaction of the α-Mg phase with the C36 phase [128]. The coupling of the primary phase with the secondary phases resulted in galvanic corrosion of both the alloy and NCs [124]. The large loops at high and mid-frequency ranges correspond to the capacitive loops, which is attributed to the charge transfer resistance at the interface of the electrolyte and working electrode. The increased loop radius of the NCs at higher frequency with increasing SiC_{np} content suggests that the charge transfer rate became slow in the NCs compared to the AXM520 alloy. The inductance loop at low-frequency region is associated with the localized corrosion by Cl^- ions and break down of the corrosion product film.

Figure 7.3(b) displays the Bode magnitude plots for all the as-cast compositions. The plots exhibit the variation of impedance magnitude (|Z|) within the chosen frequency range. The AXM520 alloy exhibited the lowest value of |Z| whereas, it was highest in NC3.0SiC. The values of |Z| for all the NCs were higher compared to the alloy. The |Z| value proportionally improved with that of the SiC_{np} wt.% in AX520. This implies that the resistance against corrosion of the AXM520 is enhanced with the added SiC_{np} reinforcement. The |Z| value exhibited in the low-frequency region showed a positive slope, implying the presence of an inductive loop. The negative slope of the variation of |Z| at the mid and high-frequency range suggests the presence of a capacitive loop. The variation of |Z| parallel to the abscissa implies the presence of pure resistance. Figure 7.3(c) presents the Bode phase plots for all the compositions corresponding to the Nyquist plot displayed in Figure 7.3(a). In the Bode phase diagram, an increase in the phase angle and width of the peak implies a higher resistance, reduced capacitance, and higher corrosion resistance [127,129,130]. In the present

investigation, the phase angle and FWHM (Full-Width Half Maxima) of the largest peak corresponding to these plots increased proportionally with the increased SiC_{np} concentration in the AXM520 alloy. The FWHM value of the AXM520 alloy is 1.81 ± 0.12, and it is 2.30 ± 0.13 for NC3.0SiC. The NC0.5SiC showed the lowest value of FWHM (1.86 ± 0.10) among the NCs. Figure 7.3(d) presents the equivalent circuit that closely matches the electrochemical behavior depicted in Figure 7.3(a to c). The impedance of the circuit that mimics the exact corrosion behavior of all the compositions is calculated from the equation:

$$Z = Z_{R_s} + \left(\frac{1}{Z_{R_l}+Z_L} + \frac{1}{\frac{Z_{R_F} Z_{CPE_F}}{Z_{R_C}+Z_C} + \frac{Z_{R_{DL}} Z_{CPE_{DL}}}{Z_{R_{DL}}+Z_{CPE_{DL}}}} \right)^{-1} \quad \text{Equation 7.2}$$

The fitted data corresponding to the elements shown in Figure 7.3(d) are summarized in Table 7.2. The values of solution resistance (R_s), were almost the same for all the materials tested (i.e.,10.91 to 11.28 $\Omega.cm^2$). The element CPE represents the nonlinear capacitance with two components, Y and n. The magnitude of n ranges from 0 to 1. As the value of n is approaching 1, it represents a more capacitive nature of the element. In the present study, the CPE_{DL} is associated with the capacitance of the electric double-layer at the interface of the NaCl solution and working electrode. The CPE_F is associated with the capacitance of the corroded film. Further, the impedance of the component (Z_{CPE}) is calculated from the equation [131]:

$$Z_{CPE} = \frac{1}{Y(if)^n} \quad \text{Equation 7.3}$$

In the above equation, Y and n are the empirical parameters as described earlier, *f* represents the frequency, and $i = \sqrt{-1}$.

From Table 7.2, it is observed that the values of Y are inversely related to SiC_{np} wt.% in the AXM520 system, and accordingly, the values of $Z_{CPE_{DL}}$ and Z_{CPE_F} increases. The electronic double layer and corrosive film provided a higher resistance during charge transfer in NCs, which resulted in the superior corrosion inhibition property of the NCs. Furthermore, the resistances of the double layer (R_{DL}) and corroded film (R_F) also increased with the increase in SiC_{np}, indicating improved corrosion performance. It implies that the corrosive films were more inert in NCs compared to the AXM520 alloy, resulting in less dissolution of the α-Mg phase [129]. The series arrangement of inductance (L) and its resistance (R_L) represents the localized corrosion of the α-Mg phase. This is attributed to the poor stability and breaking of the $Mg(OH)_2$ film [132,133]. The values of L and R_L increased as the concentration of the SiC_{np}

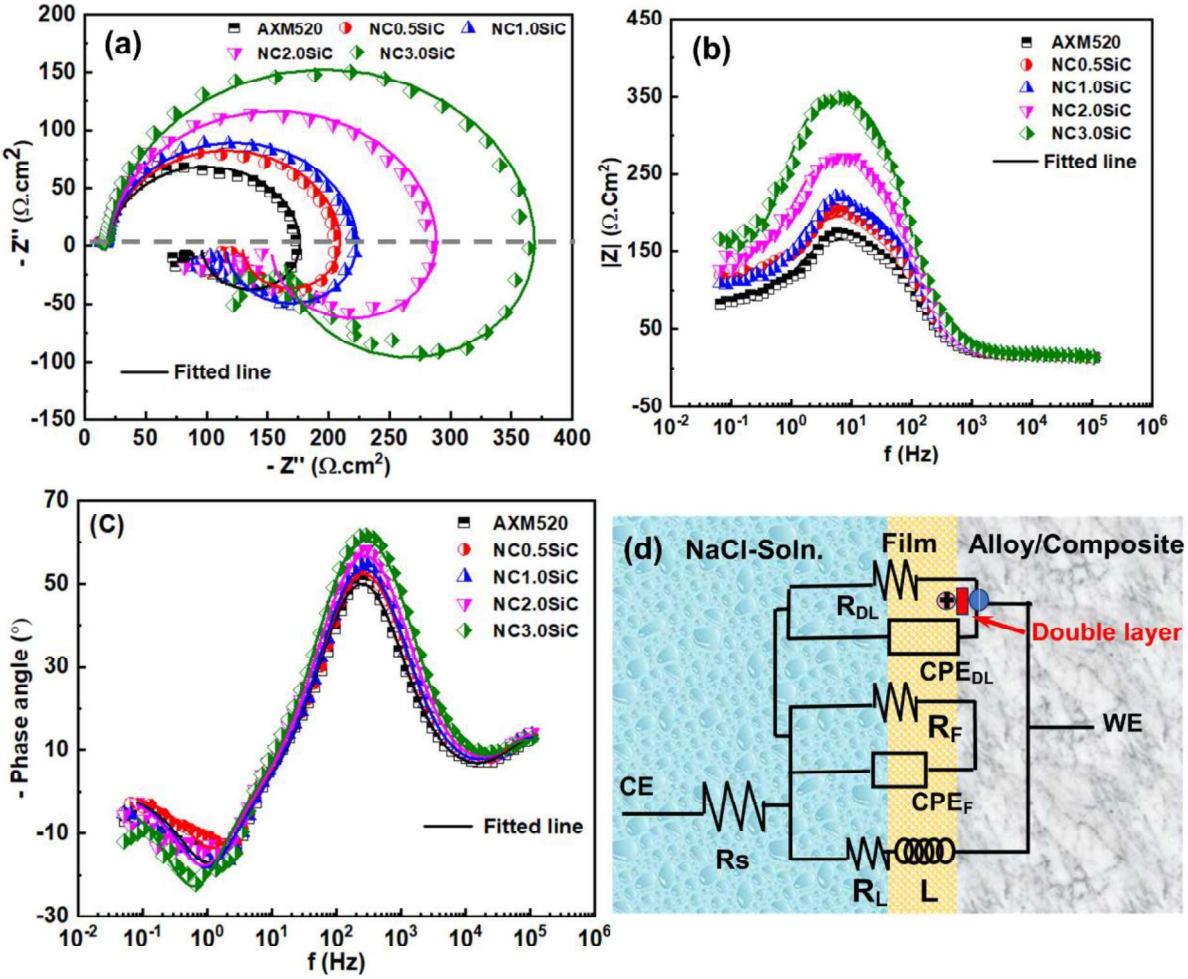

Figure 7.3 Presentation of (a) Nyquist plots, (b) impedance vs. frequency, and (c) phase angle vs. frequency Bode plots for AXM520 alloy and NCs; and (d) equivalent circuit for the observed EIS response.

increased, indicating the formation of a stable corrosion film on NCs. The polarization resistance (R_p) of the equivalent circuit is calculated using the following equation at $f = 0$ [128].

$$\frac{1}{R_p} = \frac{1}{R_F + R_{DL}} + \frac{1}{R_L} \quad \text{Equation 7.4}$$

The calculated values of R_p are enlisted in Table 7.2. The smallest magnitude of R_p for the AXM520 alloy indicates its highest corrosion rate. The values of R_p for the NCs were higher indicating their reduced corrosion rate than the alloy.

Table 7.2 Summary of the elements obtained from the equivalent circuit fitted with the experimental EIS data.

Materials	R_s ($\Omega.cm^2$)	R_{DL} ($\Omega.cm^2$)	CPE_{DL} ($F.cm^{-2}$)		R_f ($\Omega.cm^2$)	CPE_f ($F.cm^{-2}$)		R_L ($\Omega.cm^2$)	L ($H.cm^2$)	R_P ($\Omega.cm^2$)	OCP (mV)
			Y (10^{-7})	n		Y (10^{-5})	n				
AXM520	10.9±0.7	6.4±1.2	9.2±0.8	0.93±0.02	154.8±6.2	2.3±0.7	0.93±0.07	160.9±9.5	30.1±0.3	80.5	-1559.7 ± 4.8
NC0.5SiC	10.9±0.4	6.5±0.9	8.9±0.3	0.91±0.03	183.9±9.5	1.9±0.3	0.93±0.06	202.5±9.1	37.6±1.2	98.1	-1538.2 ± 5.3
NC1.0SiC	9.1±1.2	7.3±0.4	7.6±0.2	0.84±0.01	198.1±2.4	1.7±0.5	0.94±0.04	216.4±17.9	40.1±2.7	105.3	-1511.5 ± 2.7
NC2.0SiC	10.3±0.9	8.9±1.0	5.2±0.8	0.94±0.02	263.8±1.6	1.5±0.8	0.92±0.05	246.1±10.7	59.3±3.2	129.3	-1474.3 ± 6.7
NC3.0SiC	11.2±0.6	10.1±1.1	4.9±0.5	0.96±0.01	344.1±2.1	1.2±0.3	0.93±0.01	262.0±6.1	76.1±5.8	150.6	-1453.1 ± 5.3

7.4 Potentiodynamic polarization test

Figure 7.4(a) presents the Tafel plots obtained from the potentiodynamic polarization tests of the as-cast AXM520 and its NCs. The corrosion rate (mm/yr), I_{corr}, and E_{corr} were calculated from Figure 7.4(a), and their variations as a function of SiC_{np} concentration are revealed in Figure 7.4(b). The E_{corr} shifted to a more positive value, whereas the I_{corr} values dropped significantly as wt.% of dispersed SiC_{np} increased in AXM520 alloy. The corrosion rate of AXM520 alloy was highest, i.e., 0.58 ± 0.02 mm/yr. The corrosion rate of the NCs was lower than the alloy. The NC0.5SiC had a corrosion rate of 0.49 ± 0.03 mm/yr, which is highest among the NCs. The NC1.0SiC and NC2.0 exhibited a corrosion rate of 0.19 ± 0.07 and 0.11 ± 0.05 mm/yr, respectively. The NC3.0SiC showed 91.3 % (0.05 ± 0.01 mm/yr) improvement in contrast to the corrosion rate of AXM520 alloy. Thus, the additions of SiC_{np}

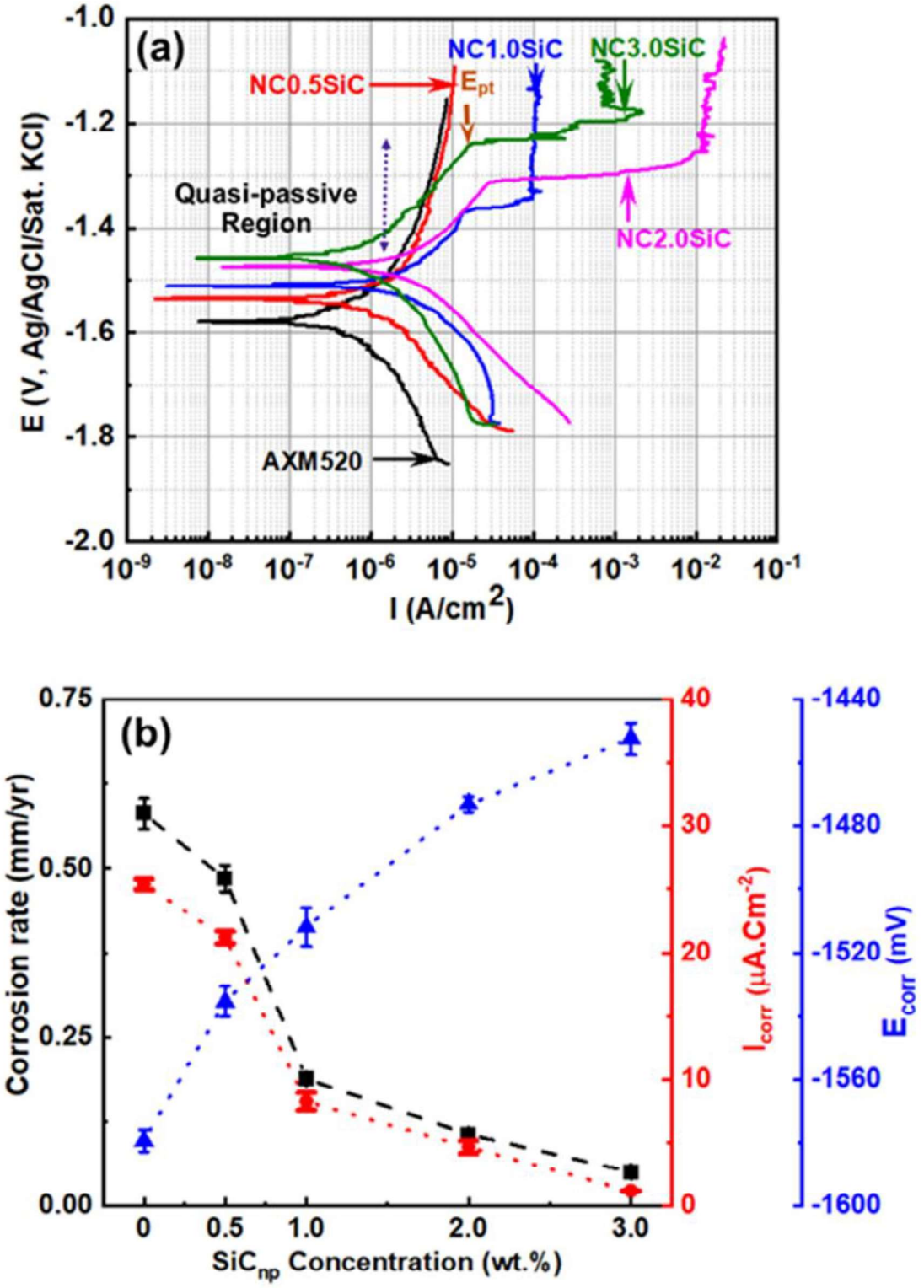

Figure 7.4 (a) Potentiodynamic polarization curves; (b) the variation of calculated Icorr, $E_{corr,}$ and corrosion rates with SiC_{np} concentration for the AXM520 alloy and NCs.

significantly inhibited the corrosion of AXM520 alloy. The improved corrosion rate of Mg alloys owing to nanoparticle addition was reported earlier as well [44,126]. Most interestingly, the anodic branch of the NC1.0SiC, NC2.0SiC, and NC3.0SiC exhibited nobler pitting breakdown potential (E_{pt}) as compared to the AXM520 and NC0.5SiC. After E_{pt} potential, all the curves exhibited a rapid increase in current density, indicating the breakdown of the semi-protective film and the rapid dissolution of the α-Mg phase. The difference between E_{corr} and E_{pt} of NC1.0SiC, NC2.0SiC, and NC3.0SiC were 141.4 ± 5.4, 173.14 ± 2.3, and 215.3 ± 2.6, respectively. The results again confirm that the resistance against pitting corrosion increased as the SiC_{np} concentration increased in the AXM520 alloy.

7.5 Volta potential measurement

The results of the hydrogen evolution tests and electrochemical corrosion tests signify that the dispersion of SiC_{np} significantly inhibited the corrosion of AXM520 alloy. Therefore, the volt potential difference between α-Mg and C36 in AXM520 alloy as well as NC3.0SiC was quantified to understand the corrosion behavior. Figure 7.5(a to d) exhibits the SKPFM results obtained from AXM520 alloy and NC3.0SiC. Figure 7.5(a and c) exhibits the volta potential maps, and Figure 7.5(b and d) portrays the variation of volta potential as a distance along the lines marked in the former images. The difference in potential between α-Mg and C36 phases at the grain boundaries was 85.29 ± 1.52 mV in AXM520, as shown in Figure 7.5(a and b). Metalnikov et al. [134] showed that the potential difference between these two phases was 140 mV in AXM610 alloy. Baek et al. [135] studied the corrosion behavior of the AZ61 with varying Ca wt.%. They reported that the potential difference between primary α-Mg and secondary C36 phase was 230 mV in AZX611 alloy. Thus, the alloy composition significantly alters the volta potential difference between the two constituent phases. In NC3.0SiC, the potential of the C36 phase was 36.95 ± 1.13 mV higher than the α-Mg phase, as displayed in Figure 7.5(c and d). The decrease in the volta potential difference was owing to the dispersion of SiC_{np} in the α-Mg phase. A significant amount of SiC_{np} was engulfed by the α-Mg phase during solidification of the NCs. Thus, the potential of the α-Mg phase is reduced by 1.6 times in the NC3.0SiC compared to that in the AXM520 alloy. The addition of nanoparticles increased the viscosity of the melt [90,91], which decreased the solid-liquid interface velocity during solidification. The decreased interface velocity entrapped a higher amount of SiC_{np} in the grain boundaries along with the C36 phase, as shown in Figure 4.7(c). These entrapped SiC_{np} in the intergranular region hindered the charge transfer between the α-Mg and C36 phases

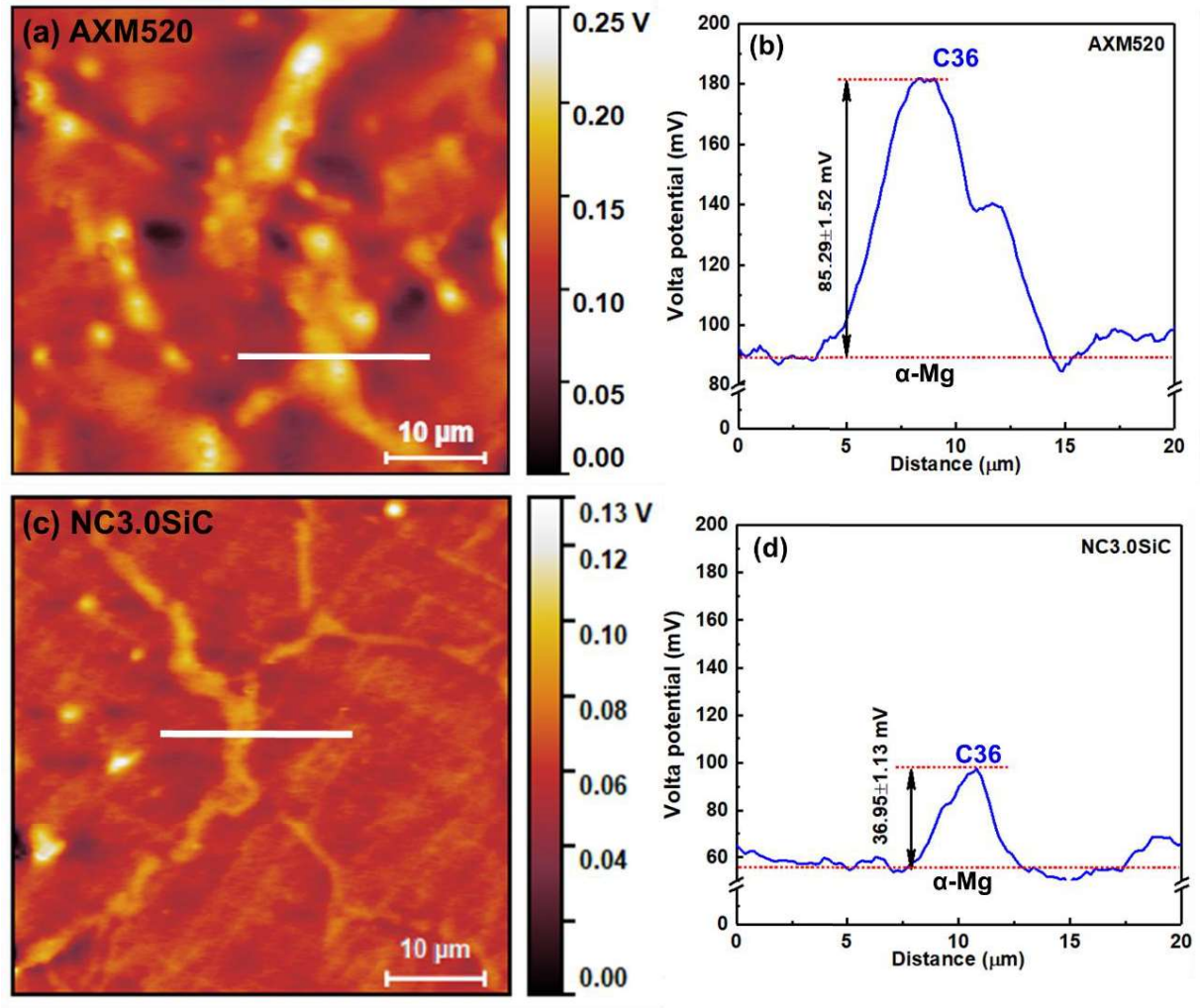

Figure 7.5 Volta potential maps for (a) AXM520 and (c) NC3.0SiC; the variation of volta potential (b and d) across the lines marked in 'a' and 'c' exhibiting the potential difference between α-Mg and $(Mg,Al)_2Ca$ (C36) phases.

owing to the poor conductivity of the SiC_{np}. Therefore, the reduced volta potential difference led to slower charge transfer between the α-Mg and C36 phase in NCs, which essentially improved the corrosion resistance of NCs with respect to AXM520 alloy. The aforementioned results further confirm the increased impedance resistance (L) in the NCs, as listed in Table 7.2. Ganguly et al., in two separate studies, concluded that adding SiC_{np} or graphene nanoparticles decreased volta potential values between α-Mg and β-$Mg_{17}Al_{12}$ phases in AZ91-based alloys, resulting in the better corrosion properties of the NCs compared to the monolithic alloy [44,126].

7.6 Characterization of corrosion film

7.6.1 SEM micrographs of corroded film

Figure 7.6(a to e) exhibits the SEM micrographs of the corroded film formed on the contact surface of AXM520 alloy and NCs following the electrochemical tests. The film primarily consists of $Mg(OH)_2$ (as confirmed by the XRD patterns discussed in section 7.6.2) which is insoluble in an aqueous medium [124,125]. The Cl^- ions in the aqueous NaCl solution attacked the $Mg(OH)_2$ layer and formed the soluble $MgCl_2$, which deteriorated the protective layer. Figure 7.6(a) exhibits the corrosion layer formed on the AXM520 alloy. The presence of excessive cracks on the corroded film is observed. However, the cracks were shallower and less visible in the NCs, as exhibited in Figure 7.6(b to e). As a result, the quantity of $Mg(OH)_2$ phase formed reduced as the SiC_{np} wt.% gradually enriched in the NCs. The EDS results obtained from the corroded films of the AXM520 alloy and NC3.0SiC are shown in Figure 7.7(a to d). It is evident that the corroded film on the NC3.0SiC contains relatively higher Al (i.e., 7.05 wt.%) than that (0.83 wt.%) of the AXM520 alloy. The higher Al content on the corrosion film of the NC3.0SiC was attributed to the higher Al content in the α-Mg phase, as discussed earlier in section 4.1 of chapter 4.

7.6.2 XRD and FTIR analysis of the corroded products

Figure 7.8(a) exhibits the XRD profile of the collected corroded products from the top of the corrosion-tested AXM520 and NCs. The presence of $Mg(OH)_2$ compound in the corrosion films of the tested alloy and NCs is confirmed. The XRD peaks corresponding to the parent α-Mg were also observed. The reaction leading to the formation of $Mg(OH)_2$ was discussed in Equation 7.1. The $MgCO_3.3H_2O$ (nesquehonite) phase was also identified in the XRD peaks of all the samples. The formation of the compound indicates that atmospheric CO_2 also plays

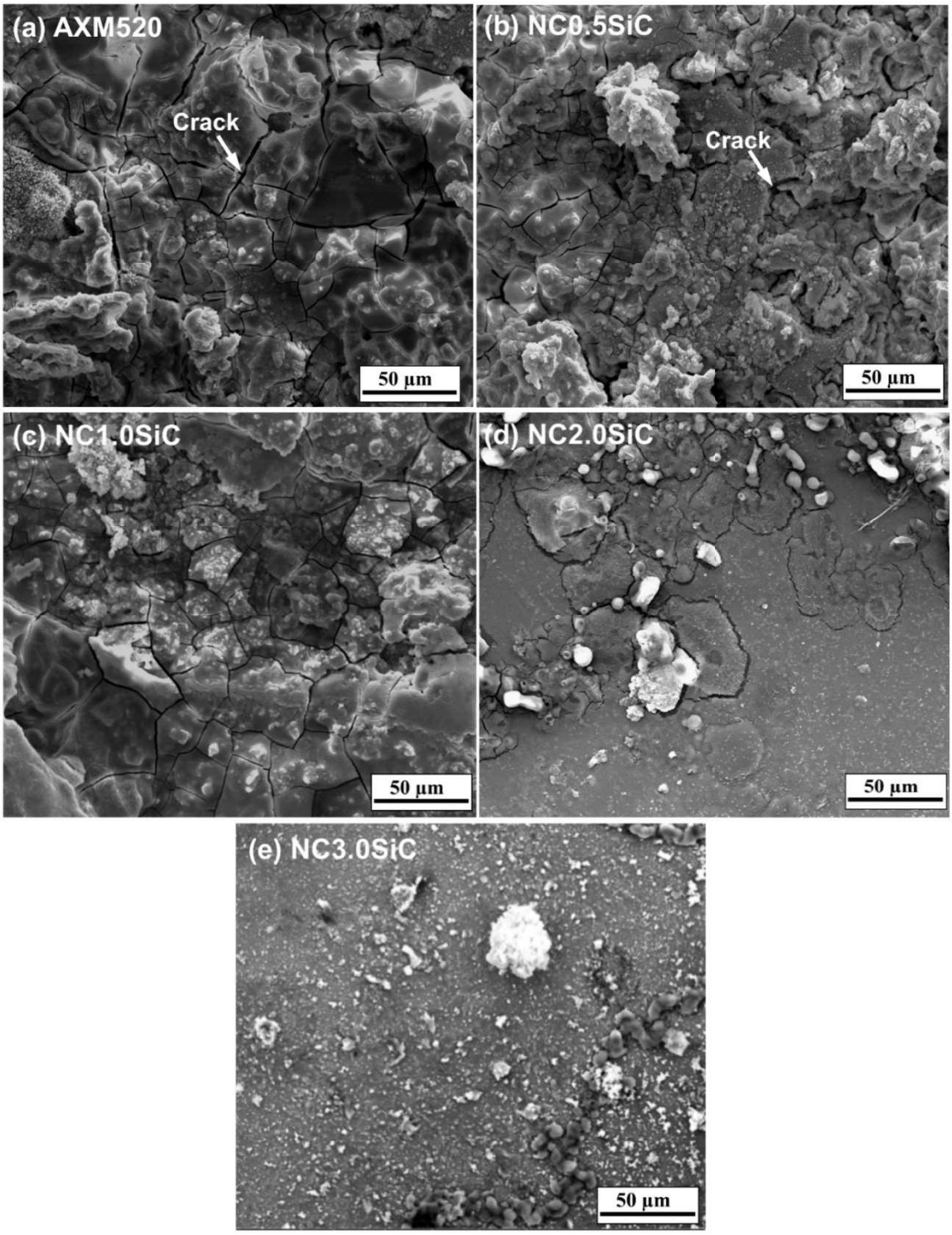

Figure 7.6 SEM images of the corrosion films formed on the surfaces of AXM520 (a) and NCs (b to e).

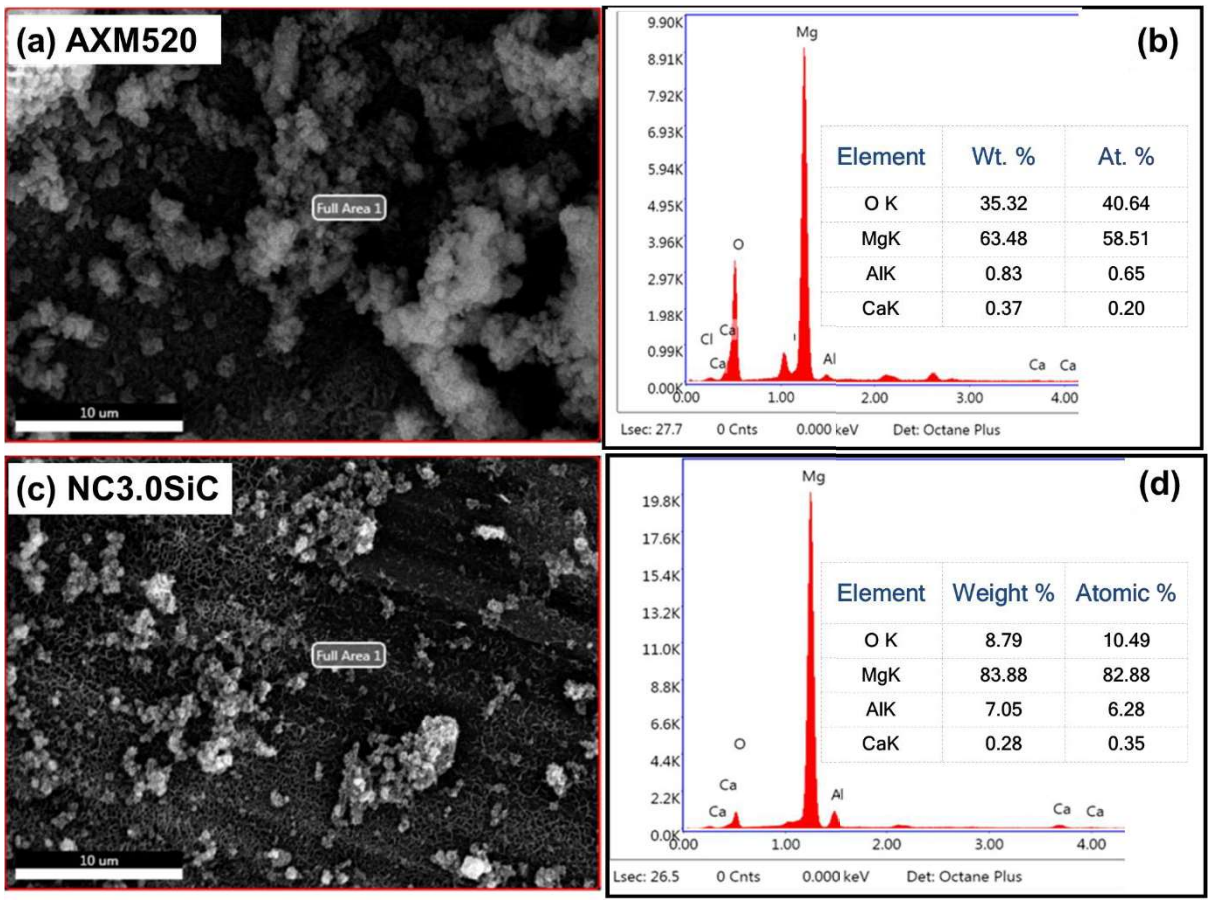

Figure 7.7 EDS results obtained from the corroded films of the AXM520 alloy (a and b) and NC3.0SiC (c and d) confirming the higher Al content on the corrosion film of the NC3.0SiC.

a significant part in the corrosion of Mg-based alloys and NCs. The CO_2 in the atmosphere reacted with $Mg(OH)_2$ as per the reaction [125,126].

$$Mg(OH)_2 + CO_2 \rightarrow MgCO_3 + H_2O \quad \text{Equation 7.5}$$

Further, $MgCO_3$ combined with H_2O present in the aqueous NaCl solution formed $MgCO_3.3H_2O$. In addition, the Layered Double Hydroxide (LDH) was also detected on the corroded films of the alloy and NCs. The LDH formation took place owing to the increased pH (~11.2) of the electrolyte [136,137]. The pH of the electrolyte increased by the dissolution of $Mg(OH)_2$ from the corroded films. Furthermore, the increase in the peak intensity of the LDH phase was attributed to the increased Al content in the α-Mg phase of the NCs. The increased LDH content resulted in an increase in the charge transfer resistance of the corroded films and was confirmed earlier by the increased corroded film resistance by EIS measurement. Thus, the increased LDH content in the corroded film might acted as a quasi-passive film on the surface of the NCs. The presence of amorphous compounds was not detected in the XRD pattern. Therefore, the possibility of formation of such compounds was checked with FTIR and XPS. Figure 7.8(b) presents the FTIR spectra recorded from the corroded film from as-cast AXM520 and NCs. The intensity of the peaks associated with the different functional groups decreased with the higher content of SiC_{np} in the as-cast AXM520 alloy. The strong peak corresponding to 3694 cm^{-1} signifies the presence of the stretching vibration mode of Mg-OH [138]. The occurrence of the bond further confirms the formation of $Mg(OH)_2$. Next to the Mg-OH band, a broad band of OH^- was also observed. The bond extended in the wave range of 3653 cm^{-1} to 2968 cm^{-1}. The intensity of the peak decreased significantly as the dispersed SiC_{np} increased in the AXM520 alloy. The band at 1641 cm^{-1} resembles to the bending vibration mode of the absorbed water molecules [139]. The peak at 1420 cm^{-1} presents a C-O vibration band of carboxyl groups [140]. The band at 645 cm^{-1} agrees with the stretching vibration mode of the Mg-C bond, confirming the presence of $MgCO_3$-type compounds [141].

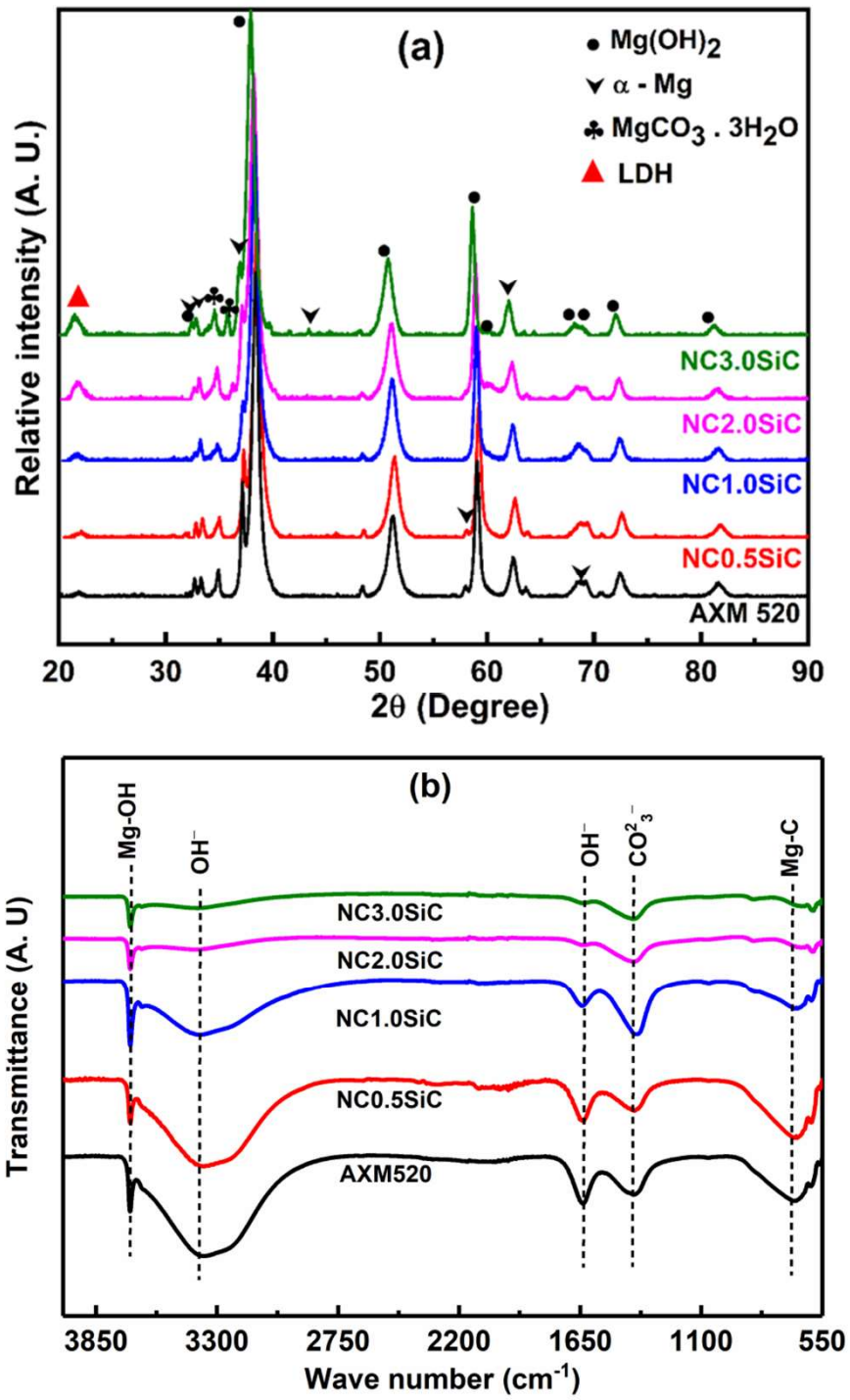

Figure 7.8 (a) XRD and (b) FTIR profiles recorded from the corroded films of all the materials tested.

7.6.3 XPS analysis

Figure 7.9(a to f) exhibits the XPS analysis acquired from the corrosion film of fabricated AXM520 and NC3.0SiC. The peaks corresponding to Mg 1s acquired from the AXM520 and NC3.0SiC are displayed in Figure 7.9(a and b), respectively. The analysis of the results shows the occurrence of $Mg(OH)_2$ and $MgCO_3$ in the corroded film. The details of the peaks are summarized in Table 7.3. The $Mg(OH)_2$ peak was observed at 1302.8 eV whereas, the peak of $MgCO_3$ was observed at 1303.7 eV. The analysis showed that the area fraction of $Mg(OH)_2$ was much higher in the corroded film of AXM520 than in the corroded layer on NC3.0SiC. Furthermore, the analysis of Al 2p peaks confirmed the presence of $Al(OH)_3$ and Al_2O_3 at 73.8 and 70.3 eV, respectively, in both the AXM520 alloy and NC3.0SiC, as displayed in Figure 7.9(c and d). The increased peak area of the $Al(OH)_3$ was might contributed by the Al-LDH layer formation, which significantly improved the corrosion resistance of the NCs. However, there is no significant change in the peaks corresponding to Ca 2p acquired from the corrosion films of AXM520 alloy and NC3.0SiC nanocomposite, as shown in Figure 7.9(e and f) [127].

Thus, the addition of SiC_{np} in the AXM520 alloy decreased the amount of corrosion products. The reduced amount of $Mg(OH)_2$ lowered the formation of $MgCl_2$. The $Al(OH)_3$ and Al-LDH layer is more stable than $Mg(OH)_2$. Thus, the stable corroded film containing more $Al(OH)_3$ and Al-LDH improved the corrosion resistance of the NCs by preventing Cl^- ions attack on the $Mg(OH)_2$ layer.

Table 7.3 Summary of the area percentage data evaluated from the XPS peaks of AXM520 and NC3.0SiC after deconvoluting.

Materials	**Mg 1s**		**Al 2p**		**Ca 2p**	
	$MgCO_3$ (1303.7 eV)	**$Mg(OH)_2$** (1302.8 eV)	**$Al(OH)_3$** (73.8 eV)	**Al_2O_3** (70.3 eV)	**CaO** (354.5 eV)	**$Ca(OH)_2$** (351.7 eV)
AXM520	25.0	70.9	26.6	73.4	5.2	94.8
NC3.0SiC	42.1	57.9	50.6	49.5	5.8	94.2

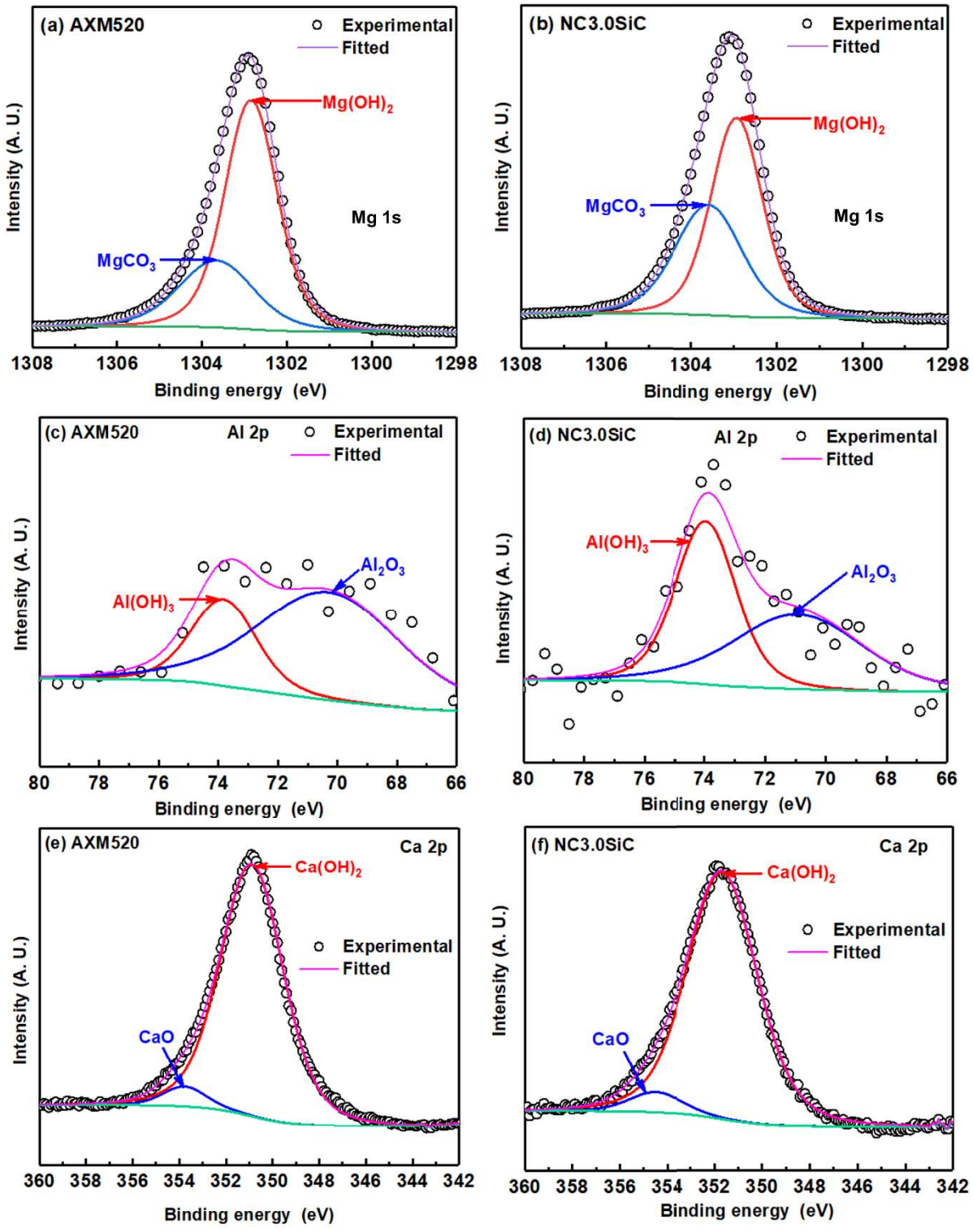

Figure 7.9 XPS spectra acquired from the corroded films of AXM520 (a, c, e) and NC3.0SiC (b, d, f).

7.7 Characterization of corroded surfaces

The corroded surfaces of as-cast AXM520 and NCs were analyzed after removing the corroded film with a standard chromate solution. Figure 7.10(a to e) shows the topological map of the corroded surfaces of AXM520 and NCs after the removal of accumulated corroded films. The results were subsequently analyzed using Gwyddion software to estimate the roughness of the corroded surfaces. The roughness values of all the compositions as a function of SiC_{np} are shown in Figure 7.10(f). The roughness values of the corroded surfaces inversely varied with respect to the SiC_{np} wt.% in AXM520 alloy. The AXM520 alloy showed the highest roughness value of 17.7 ± 2.7 μm among the compositions. The roughness value of the NC0.5SiC, i.e., 14.2 ± 4.9 μm, was the highest among the NCs. The lowest roughness value i.e., 3.1 ± 1.3 μm, was for NC3.0SiC. Therefore, adding 3.0 (wt.%) of SiC_{np} in as-cast AXM520 alloy reduced the corroded surface roughness of AXM520 alloy by 82.5%.

Figure 7.11(a) depicts the corroded surface of the as-cast AXM520 alloy observed under SEM. The elemental mapping related to Figure 7.11(a) is displayed in Figure 7.11(b). The image confirms that certain regions were deeply corroded, and these regions are surrounded by boundary walls. The deeply corroded regions corresponded to the primary α-Mg phase, and the boundary walls were the secondary C36 phase, as confirmed in the elemental mapping. This suggests that galvanic corrosion occurred between these phases. Thus, the α-Mg phase acted as an anode while the C36 phase at the interfaces of different grains acted as a cathode during the galvanic corrosion. The morphologies of the corroded surfaces in the NCs are shown in Figure 7.11(c to f). The depth of the corroded α-Mg phase reduced significantly with the higher content of SiC_{np} wt.% in as-cast AXM520 alloy. The relative potential between these two phases is reduced with the increased SiC_{np} wt.% in the NCs, which subsequently reduced the galvanic corrosion rate and improved the corrosion resistance of as-cast NCs. Figure 7.12(a and b) exhibits the cross-sectional views of the AXM520 alloy and NC3.0SiC after the removal of the corrosion products. The depth of the corroded layer in the AXM520 alloy (i.e., 164.6 μm) is 2.9 times higher than that (i.e., 57.4 μm) in the NC3.0SiC confirming the severe corrosion of the AXM520 alloy as compared to the NCs.

The schematics of the corrosion mechanism involved in the as-cast AXM520 and NC3.0SiC (representative for the NCs) are presented in Figure 7.13(a and b). In stage I, the $Mg(OH)_2$-rich corrosion film formed on the AXM520 alloy, as depicted in Figure 7.13(a). The $Mg(OH)_2$ film

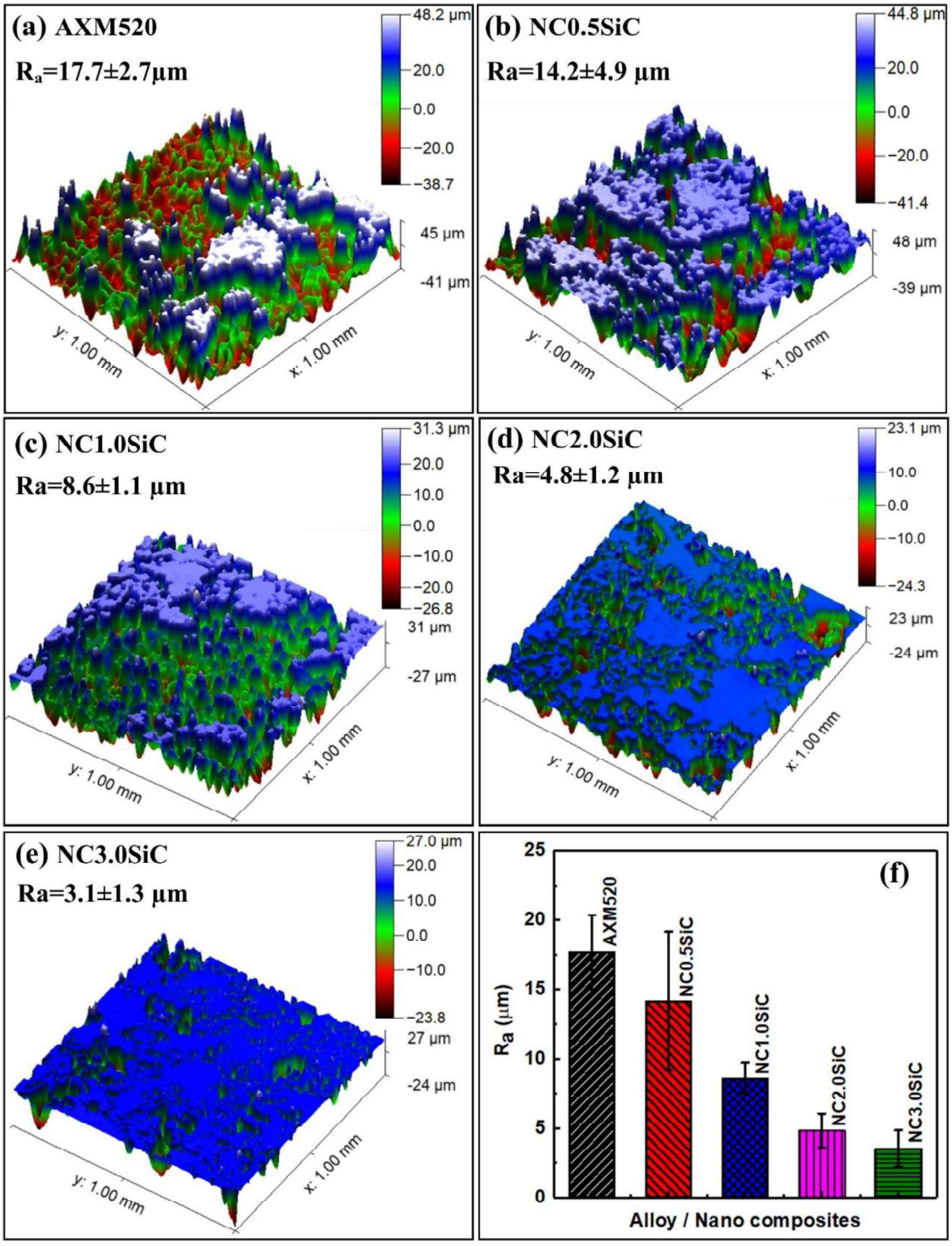

Figure 7.10 3D presentation of corrosion products free surface morphologies of AXM520 (a) and NCs (b to e); summary of surface roughness values (f).

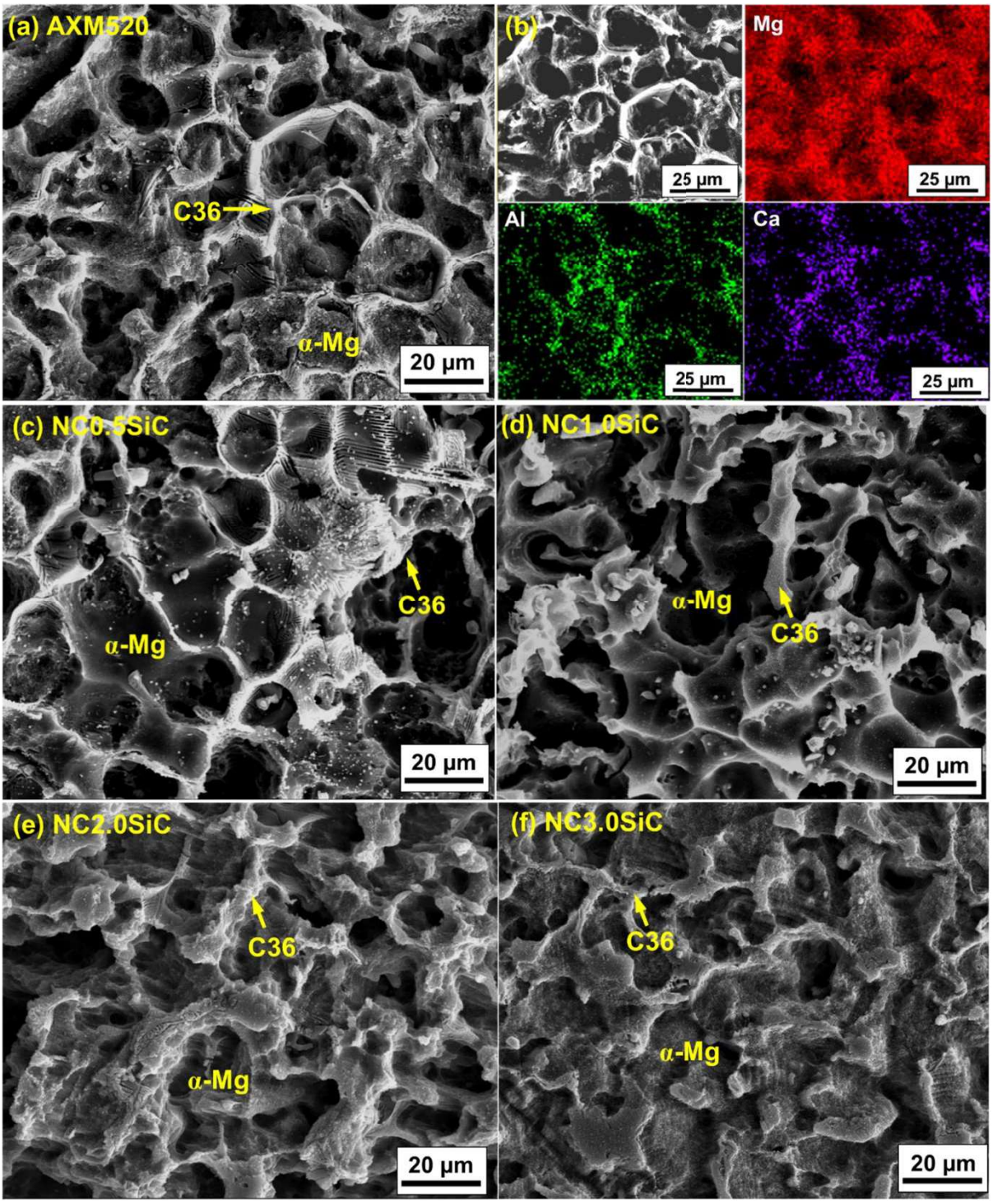

Figure 7.11 SEM micrographs of corrosion products free surfaces of AXM520 with elemental mapping (a and b), and NCs (c to f).

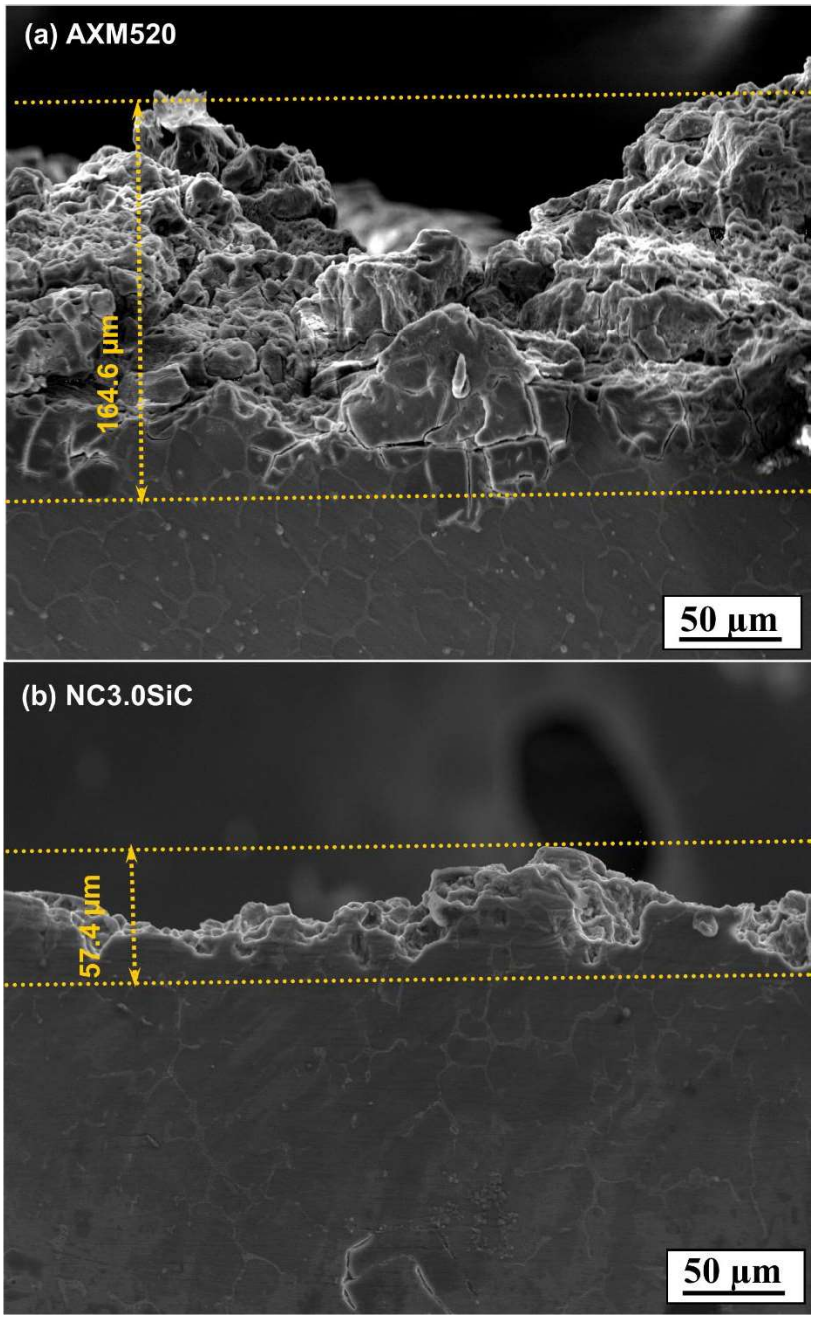

Figure 7.12 Cross-sectional micrographs of the corroded surfaces of the (a) AXM520 alloy and (b) NC3.0SiC depicting the extent of corrosion.

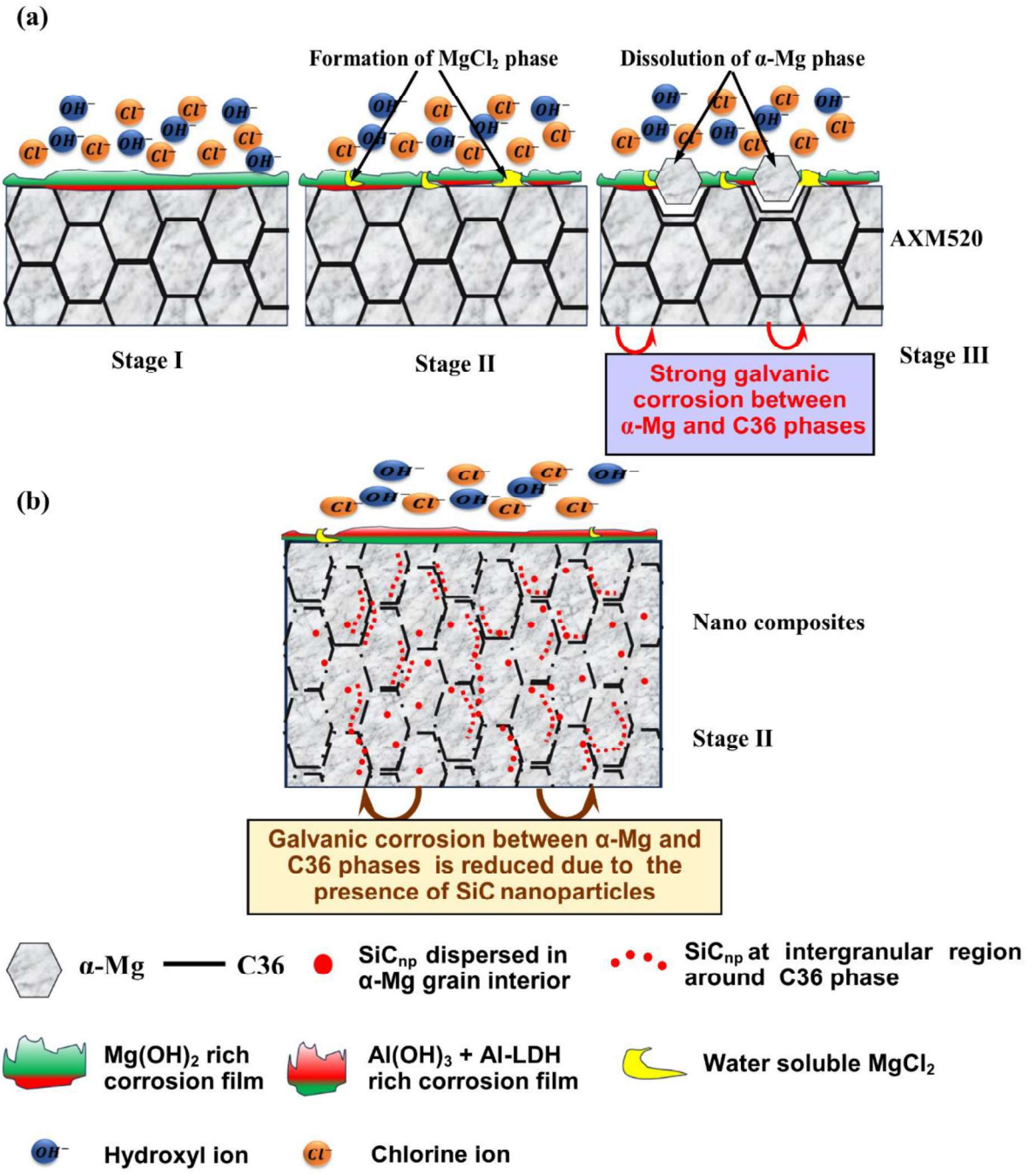

Figure 7.13 Schematic representation showing the different stages of corrosion mechanism took place in (a) AXM520, and (b) NC3.0SiC.

was attacked by Cl^- ion present in the NaCl solution and aqueous soluble $MgCl_2$ formed in stage II. Thus, the $Mg(OH)_2$ film became unstable. In stage III, the dissolution of the α-Mg phase took place due breaking of $Mg(OH)_2$ layer. However, the reduced volta potential difference between α-Mg and C36 phases minimized the extent of galvanic corrosion in NC3.0SiC. The reduced volta potential between α-Mg and C36 is attributed to the formation of non-conducting SiC_{np} layer around the C36 phase, that leads to decrease galvanic potential between α-Mg and C36 phase, as discussed earlier in section 7.5. For the NC3.0SiC, the amount of formation of $Mg(OH)_2$ is reduced, and accordingly the $Al(OH)_3$ and Al-LDH-rich corroded film is formed, as shown in Figure 7.13(b). The Al-LDH-rich film is more stable than the $Mg(OH)_2$-rich film contributing to better corrosion resistance of the NCs.

7.8 Summary of chapter 7

In this chapter, the corrosion behavior of squeeze-cast Mg-5.0Al-2.0Ca-0.3Mn (wt.%) (AXM520) alloy and nanocomposites are presented. The major findings from the current chapter are summarized below.

i. The corrosion resistance of the NCs measured in the hydrogen evolution test was superior to the AXM520 alloy, and the improvement was 91.1% in the NC3.0SiC.

ii. The OCP of all NCs shifted to more noble values with the increased quantity of SiC_{np} in AXM520. The polarization resistance determined from the EIS increased with the increase in the SiC_{np} content in the NCs.

iii. The potentiodynamic polarization scans further confirmed the superior corrosion resistance of the NCs to the AXM520 alloy. Among the fabricated NCs, NC3.0SiC exhibited the highest corrosion resistance, and it was 91.3% lower in comparison to the AXM520 alloy.

iv. The corrosion products predominantly consist of $Mg(OH)_2$. The addition of SiC_{np} reduced the formation of $Mg(OH)_2$ and increased the content of the $Al(OH)_3$ in the NCs leading to the higher stability of the corroded film formed on them.

v. The α-Mg phase was severely damaged owing to the galvanic corrosion between the α-Mg and C36 phases. However, the galvanic corrosion was reduced due to a decrease in the volta potential between α-Mg and C36 phases in the NCs, resulting in their superior corrosion resistance.